Electron-helium scattering in Debye plasmas

Mark C. Zammit,[1,*] Dmitry V. Fursa,[1] Igor Bray,[1] and R. K. Janev[2]
[1]*ARC Centre for Antimatter-Matter Studies, Curtin University, GPO Box U1987, Perth, WA 6845, Australia*
[2]*Macedonian Academy of Sciences and Arts, P.O. Box 428, 1000 Skopje, Macedonia*
(Received 22 September 2011; published 7 November 2011)

Electron-helium scattering in weakly coupled hot-dense (Debye) plasma has been investigated using the convergent close-coupling method. The Yukawa-type Debye-Hückel potential has been used to describe plasma Coulomb screening effects. Benchmark results are presented for momentum transfer cross sections, excitation, ionization, and total cross sections for scattering from the ground and metastable states of helium. Calculations cover the entire energy range up to 1000 eV for the no screening case and various Debye lengths (5–100 a_0). We find that as the screening interaction increases, the excitation and total cross sections decrease, while the total ionization cross sections increase.

DOI: 10.1103/PhysRevA.84.052705 PACS number(s): 34.80.Dp, 52.20.Fs

I. INTRODUCTION

In the past decade, studies of hot-dense plasmas have seen an increased interest from the scientific community [1–7]. Studies of such plasmas have mainly concentrated on the research of laser-produced plasmas, astrophysics, fusion, spectroscopy, plasma, and atomic physics. It is important to investigate the atomic collisions processes in plasmas due to their use in calculating ion stage abundance and radiative power losses of the plasma, which directly effects the plasma transport properties. The spectroscopic information obtained to identify plasma temperature and pressure is also affected by atomic collision processes.

Hot-dense plasmas exhibit Coulomb screened interactions, which is a collective, many-particle effect. In the approximation of pair-wise correlations, this interaction reduces to the Yukawa-type Debye-Hückel potential [8], which is dependent on the temperature and density of the plasma. The Debye-Hückel potential of an ion of positive charge Z, which interacts with an electron, is given by

$$V(r) = -\frac{Ze^2}{r}\exp\left(-\frac{r}{D}\right), \tag{1}$$

where D is the Debye screening length $D = \sqrt{k_b T_e/4\pi e^2 n_e}$, k_b is the Boltzmann constant, T_e is the electron temperature, and n_e is the electron density. The interaction potential given by Eq. (1) is accurate if the Coulomb coupling parameter Γ and nonideality parameter γ are such that $\Gamma \leqslant 1$ and $\gamma \ll 1$, where $\Gamma = e^2/ak_bT_e$, with $a = (3/4\pi n_e)^{1/3}$ being the average interparticle distance and $\gamma = e^2/Dk_bT_e$.

Sil *et al.* [9] have investigated the different plasma models for weakly and strongly coupled hydrogen- and helium-like ion plasmas. Weakly and strongly coupled plasmas can be expressed via the Debye-Hückel and ion sphere (IS) potentials, respectively. Results were presented for structure, oscillator strengths, polarizabilities, and transition probabilities for plasmas under different coupling strengths. It was concluded that the Debye and IS models reasonably predict spectral line positions [9].

It has been shown that the Debye-Hückel potential Eq. (1) can lead to significant modification of the electron-atom scattering processes by affecting the atomic structure [9–20] and excitation dynamics [21–28].

It is well known that the screened Coulomb potential Eq. (1) can only support a finite number of bound states. Rogers *et al.* [10] investigated the one electron atom and ion energy levels in Debye plasmas. Kar and Ho have performed accurate calculations on the helium atom energy levels [11] using the Debye-Hückel potential. These studies found that with a decrease of Debye length the bound state energies increase while the target wavefunctions peaks decrease, broaden, and become more diffuse. It was also shown that a finite Debye length lifts the n,l degeneracy of the Coulomb potential. For two electron targets such as the H^- ion, the electron-electron screened interaction has been investigated by Ugalde *et al.* [19]. It was found that the two-electron correlation energy decreases as the screening increases.

Oscillator strengths and polarizabilities have been studied for one-electron [20,21] and two-electron targets [12]. Oscillator strengths were found to decrease and polarizabilities were found to increase with an increase of screening.

Several studies have been performed on doubly excited state atoms and ions. Kar and Ho [13–15] have investigated resonance states of the H^- ion interacting with a screened Coulomb (Yukawa-type) potential using the stabilization method. Doubly excited states of helium have been investigated by Saha *et al.* [16,17] and Kar and Ho [18].

Electron scattering in Debye plasmas has mainly concentrated on hydrogen-like targets. Ghoshal and Ho [26] have researched low-energy electron scattering off hydrogen atoms using a Yukawa-type potential. The highly correlated and variationally determined wavefunctions for H^- ions in plasmas are used to determine the effective range of the states. Ghoshal and Ho find that as the screening increases the elastic cross section (CS) increase at energies below the $n = 2$ excitation threshold. Recently, Zhang *et al.* described low-energy electron-hydrogen scattering using the R-matrix method concentrating on Feshbach resonances near the $n = 2$ [22,23] and $n = 3$ [24] excitation threshold regions. High-energy electron-hydrogen excitation processes have been investigated by Qi *et al.* [21] and Hatton *et al.* [27] using

*mark.zammit@student.curtin.edu.au

the first Born approximation (FBA). A study of excitation and ionization processes was performed by Zammit *et al.* [28] for electron-hydrogen scattering over the energy range from threshold to high energies (250 eV) for various Debye lengths. Conclusions drawn from these studies find that the excitation integrated CS and total cross sections (TCS) decrease with a decrease of Debye length, while the total ionization cross sections (TICS) increase with an increase of screening.

A preliminary study was conducted by Zammit *et al.* for electron-helium ground-state scattering for ionization and excitation up to the $n = 2$ states, in Debye plasmas [29]. The purpose of the present study is to investigate the effects of a Debye plasma environment on the electron-helium scattering system using the convergent close-coupling (CCC) method [30–35]. Benchmark results are presented for scattering from the ground and metastable states for excitation up to the $n \leqslant 3$ states and ionization collision processes across a broad range of incident electron energies and Debye radii.

The paper is structured as follows. The next section describes the changes made to the CCC theory to include the Debye-Hückel potential Eq. (1). Results of our calculations are presented in Sec. III for the target structure and for the various CS: integrated CS, TICS, TCS, and momentum transfer (MTCS). The conclusion is given in Sec. IV. Atomic units are used throughout the paper, unless specified otherwise.

II. METHOD

The CCC method for electron-helium scattering has been discussed in detail by Fursa and Bray [30]. Briefly, the Sturmian (Laguerre) basis is used to construct one-electron orbitals, which are then used to build a two-electron basis. The two-electron basis is used to diagonalize the helium atom Hamiltonian H_T under Debye screening

$$H_T = H_1 + H_2 + V_{12}, \tag{2}$$

where

$$H_i = -\frac{1}{2}\nabla_i^2 - \frac{Z}{r_i}\exp\left(-\frac{r_i}{D}\right), \tag{3}$$

for $i = 1,2$, is the one-electron Hamiltonian for the He^+ ion ($Z = 2$), and the electron-electron potential has the form

$$\begin{aligned} V_{ij} &= \frac{1}{|r_i - r_j|}\exp\left(-\frac{|r_i - r_j|}{D}\right) \\ &= -\frac{1}{D}\sum_{l=0}^{\infty}(2l+1) j_l\left(\frac{ir_<}{D}\right) h_l^{(1)}\left(\frac{ir_>}{D}\right) P_l\cos(\theta). \end{aligned} \tag{4}$$

For the unscreened Coulomb case ($D \to \infty$) it reduces to the well-known expression

$$V_{ij} = \frac{1}{|r_i - r_j|} = \sum_{l=0}^{\infty}\frac{r_<^l}{r_>^{l+1}} P_l\cos(\theta). \tag{5}$$

Here, $r_< = \min(r_i,r_j)$, $r_> = \max(r_i,r_j)$, P_l, j_l, and $h_l^{(1)}$ are the Legendre polynomials, spherical Bessel, and Hankel functions of the first kind, respectively. To accurately calculate j_l and $h_l^{(1)}$ with complex arguments, the subroutine COULCC developed by Thompson and Barnett [36] was used.

This diagonalization results in a set of N positive- and negative-energy square-integrable pseudostates $\Phi_n^{(N)}(x_1,x_2;D)$,

$$\left\langle \Phi_f^{(N)}(x_1,x_2;D)\right| H_T \left|\Phi_i^{(N)}(x_1,x_2;D)\right\rangle = \varepsilon_f^{(N)}\delta_{fi}, \tag{6}$$

where x is used to denote the spin and spatial coordinates. With increasing N, the negative-energy pseudostates converge to true eigenstates and the positive-energy states provide an increasingly dense discretization of the continuum. For the Coulomb potential, diagonalization using a two-electron basis allows us to represent the infinite number of discrete spectrum states and continuum via a finite number of pseudostates, which makes subsequent scattering calculations feasible. In the case of the screened Coulomb potential the discrete spectrum contains a finite number of states, which substantially changes the character of the problem from the no screening case.

The set of pseudostates is then used to perform an expansion of the total wavefunction for the electron-helium scattering system and formulate a set of close-coupling equations for the T matrix [30]. The CCC method solves the close-coupling equations in momentum space and uses the calculated T matrix to determine CS and other observables of interest.

Relatively minor modifications to the CCC method are required in order to describe electron-helium scattering in Debye plasmas. The electron-helium Hamiltonian H under Debye screening is

$$H = H_T + H_0 + V_{01} + V_{02}, \tag{7}$$

where index 0 corresponds to the projectile space. By making the simple substitutions of Eqs. (1) and (4) in place of the unscreened Coulomb potential, the CCC method formulation presented in Ref. [30] remains valid for electron scattering in Debye plasmas.

III. RESULTS

A. Target structure

In the case of helium, we need to allow for expansion over the two electrons of the target. Fortunately, all of the discrete states are sufficiently accurately described by restricting the "inner" electron to be treated by the He^+ $1s$ orbital (frozen core model). An exponential cut-off parameter $\lambda_l = 1.5$ in the Laguerre basis [30] has been used to generate the orbitals for the "outer" electron. The largest error in doing so arises for the ground state, which has an ionization error of 0.84 eV. This may be readily improved by just adding a short-ranged $\lambda_1 = 4$, $2p^2$ configuration to reduce the error to 0.35 eV and an additional $\lambda_0 = 4$, $2s^2$ configuration reduces the ground state energy error to only 0.22 eV. Using these short-ranged configurations and a Laguerre basis of the size $N_l = 20 - l$ for $l \leqslant l_{\max} = 3$, the 153 states were generated. This basis is used for calculating the CS of all the scattering processes presented, unless stated otherwise. Further improvement is of course possible, but at the cost of a considerable increase in the number of states generated, upon diagonalization of the target Hamiltonian.

Upon diagonalization of the helium atom Hamiltonian, we give the energies arising in 153-state CCC calculations for various values of D in Fig. 1 and Table I. We see that by

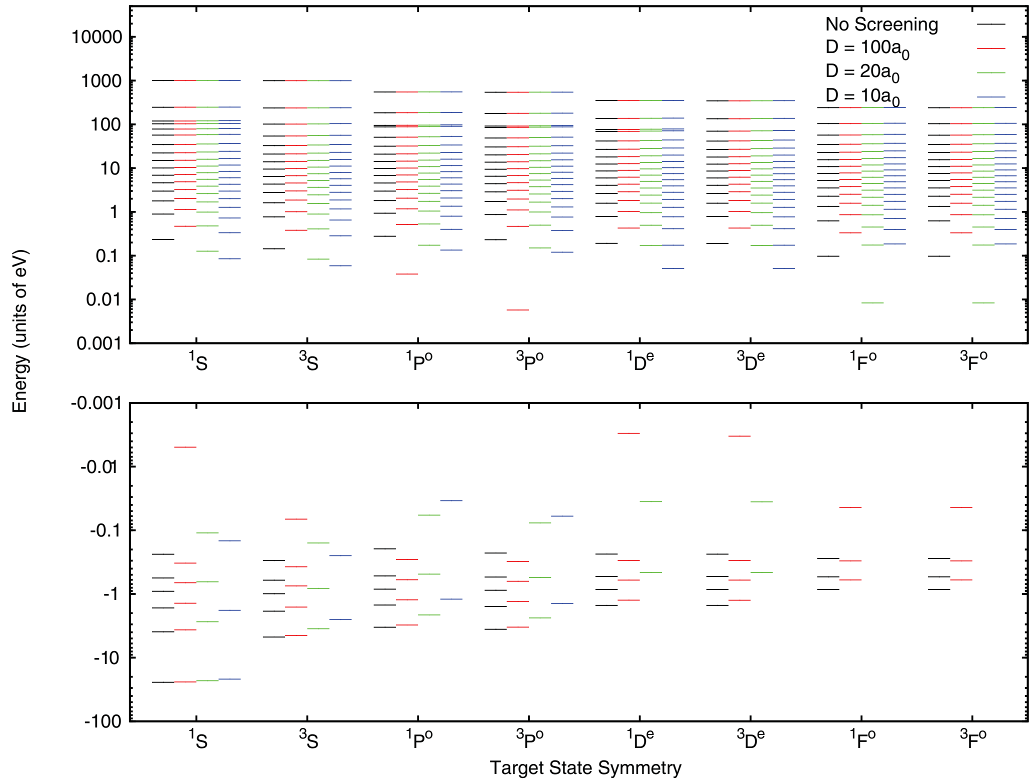

FIG. 1. (Color online) Continuum and bound-state energies of the helium atom in the 153-state CCC calculations for indicated values of Debye length.

decreasing D, the one-electron ionization energies decrease. Even for $D = 100a_0$, the difference with the no-screening case of the 2^1P level is quite substantial.

In Figs. 2 and 3 we present the 153-state CCC calculations $1^1S, n = 2$ and 3 bound-state energies versus Debye length. As the screening increases, the bound-state energies rise and enter into the continuum. The critical Debye length (D^C_α) at which the state (α) moves into the continuum is at $D^C_{1^1S} = 0.6a_0$; for the 1^1S state, refer to Fig. 2. Referring to Figs. 2 and 3, the critical Debye lengths at which the states of $n = 2$ and $n = 3$ manifolds enter the continuum are distributed in the ranges 2.5–4.6a_0 and 6.3–11a_0, respectively. It is important to note in these figures that the energy difference between states with same total angular momentum L but different spins, decrease with decreasing D. At large values of D this is also true for the states with the same spin but different L; this rule, however, may not hold for the lower D values due to the rapid changes of the energy gradient as a function of D, especially when

TABLE I. One-electron ionization energies (units of eV) of the $n \leqslant 2$ helium states for 153-state CCC calculations. Energies compared with calculations of Kar and Ho [11] for Debye lengths D (units of a_0) and experimental data [37] for $D = \infty$.

D	1^1S	2^3S	2^1S	2^3P	2^1P
∞	24.369	4.741	3.927	3.589	3.333
	24.587[b]	4.767[b]	3.971[b]	3.622[b]	3.368[b]
100	24.098	4.475	3.662	3.323	3.067
	24.32[a]	4.502[a]	3.707[a]	3.358[a]	3.105[a]
20	23.036	3.516	2.728	2.372	2.131
	23.257[a]	3.542[a]	2.771[a]	2.404[a]	2.166[a]
10	21.755	2.528	1.806	1.409	1.208
	21.975[a]	2.551[a]	1.844[a]	1.438[a]	1.236[a]
7.5	20.929	1.982	1.32	0.895	0.728
5	19.341	1.122	0.607	0.162	0.081
	19.558[a]	1.139[a]	0.634[a]	0.177[a]	0.094[a]
3.5	17.423	0.402	0.108		
2.5	15.067				

[a]Kar and Ho [11].
[b]Moore [37].

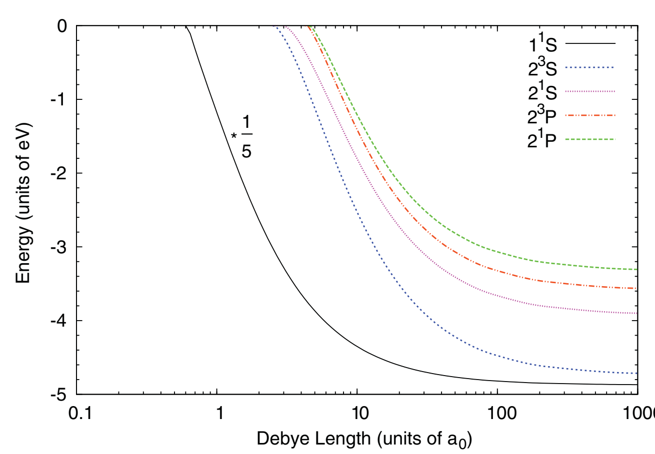

FIG. 2. (Color online) One-electron energies of the helium atom 1^1S and $n = 2$ bound states.

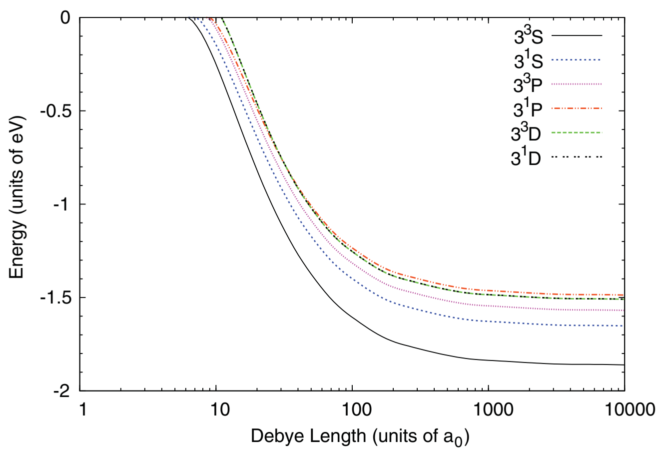

FIG. 3. (Color online) One-electron energies of the $n = 3$ helium atom bound states.

they approach the critical values D_{α}^{C}. It is to be noted that the energy of 3^1P state at $D = \infty$ lies above those of the $3^{1,3}D$ states, at $D \sim 30a_0$ the 3^1P state intersects the energies of $3^{1,3}D$ states and lies below them. This phenomenon has important implications for the electron transition processes between these two groups of states. For example, the radiative $3^1D \to 3^1P$ transition is possible only in the $11a_0 \leqslant D \leqslant 30a_0$ range.

In Fig. 4 the 153-state CCC $\langle r^2 \rangle$ value of the helium atom ground state are presented for a range of Debye lengths. We see that the electrons become further away from the nucleus as the Debye length decreases.

The correlation energy of the electron-electron potential for the ground state is given by

$$E_{\text{corr.}} = E_{He} - 2E_{He^+}, \tag{8}$$

where E_{He} is the two-electron energy. The 153-state CCC calculations ground state correlation energy is presented in Table II, for various Debye lengths. The helium atom's decrease of interelectron correlation energy when D decreases is intuitively understandable. The relative contribution increase of interelectron correlation energy to the total binding energy of helium, when D decreases, is a result of the fact for very small values of D both electrons are close to the continuum edge and their mutual interaction is stronger than that with the nucleus.

In Table III we present the 153-state CCC oscillator strengths and compare them with the accurate calculations of Kar and Ho [18]. The decrease of $1^1S \to 2^1P$ and the increase of $2^1S \to 2^1P$ and $2^3S \to 2^3P$ oscillator strengths when D decreases are observed in Table III and are related, respectively, to the energy difference decrease of 1^1S and 2^1P states and to the increase of the overlap of the wavefunctions in the $n = 2$ manifold when D decreases.

In Table IV we present the 153-state CCC static dipole polarizability of the ground state and compare them with the calculations of Kar and Ho [18]. In Fig. 5 we present the ground and metastable states dipole polarizability of the 153-state CCC calculations, the ground state is compared with the calculations of Kar and Ho [18] over a range of Debye lengths. The strong increase of the continuum contribution to the static dipole polarizability with decreasing D is related to the successive entering of discrete n, P states into the continuum as D decreases. For $D < 3.5a_0$ there are no bound P states in the discrete spectrum (see Table I) and the dipole polarizability of ground state helium atom is determined by its dipole coupling with the continuum only. It should also be noted that the contribution of the discrete spectrum to dipole polarizability decreases with decreasing D (see also [20]). The 153-state CCC basis produces the dipole polarizability more accurately as D decreases.

B. Scattering results

1. *Excitation and ionization cross sections of the ground state*

We performed 153-state CCC calculations over the entire energy range up to 1000 eV for Debye lengths $D \geqslant 5a_0$. To speed up convergence of the partial wave expansion, the CCC method uses the analytic Born subtraction technique. Around 20 partial waves were required to obtain convergence at the largest considered energy. Convergence for the no-screening results were demonstrated by Fursa and Bray [30,32], who preformed smaller calculations than those used here. All

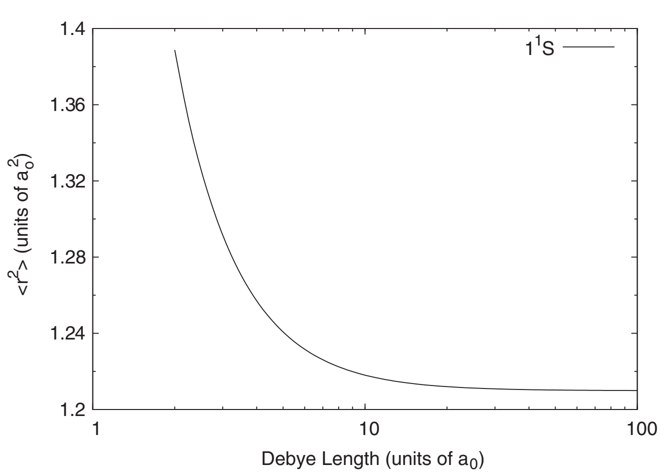

FIG. 4. 153-state CCC $\langle r^2 \rangle$ values of the He atom ground state.

TABLE II. 153-state CCC calculations complete ground-state two-electron energy (units of eV) of the He(1^1S) and He$^+$($1s$) targets and the electron correlation energy of the helium atom as described by Eq. (8), for various Debye lengths D (units of a_0).

D	He(1^1S)	He$^+$($1s$)	$E_{\text{corr.}}$	% Corr.
∞	−78.8	−54.4	30.1	38
100	−77.9	−53.9	29.8	38
20	−74.8	−51.8	28.7	38
15	−73.5	−50.9	28.3	38
10	−70.9	−49.2	27.4	39
7.5	−68.4	−47.5	26.6	39
5	−63.6	−44.3	24.9	39
2.5	−50.6	−35.6	20.5	40
2	−44.8	−31.7	18.5	41
1.5	−36.2	−25.8	15.4	42
1	−22.0	−16.1	10.2	46

TABLE III. 153-state CCC calculations oscillator strengths for transitions involving the $n = 1, 2$ levels in helium, as obtained in the length (L) and velocity (V) gauges for various Debye lengths D (units of a_0). Results compared with the calculations of Kar and Ho [18].

	$1^1S \to 2^1P$			$2^1S \to 2^1P$			$2^3S \to 2^3P$		
D	L	V	[18]	L	V	[18]	L	V	[18]
∞	0.266	0.271	0.276	0.384	0.349	0.376	0.555	0.565	0.539
100	0.265	0.271	0.275	0.384	0.350	0.377	0.555	0.565	0.539
20	0.252	0.258	0.262	0.403	0.369	0.396	0.570	0.580	0.554
15	0.243	0.248	0.253	0.417	0.384	0.409	0.581	0.591	0.565
10	0.218	0.223	0.227	0.456	0.424	0.448	0.610	0.620	0.594
5	0.093	0.095	0.099	0.663	0.641	0.656	0.724	0.733	0.715

results presented are from 153-state CCC calculations, unless specified otherwise.

To demonstrate convergence we have compared the 153-state CCC calculations to a 110-state CCC calculation for the no-screening and $D = 10a_0$ cases for two observables. The 110-state calculations were obtained by taking short-ranged $1s^2$ and $2p^2$ configurations with a Laguerre basis size $N_l = 15 - l$ for $l \leqslant l_{\max} = 3$. In Fig. 6, we present ground-state scattering TICS and in Fig. 7 we present the $1^1S \to 3^1P$ excitation. We see that the two calculations have converged to the same result across all energies. These results will be discussed in further detail below.

The ground-state excitation integrated CS up to $n = 2$ states are presented in Fig. 8, including the ground-state TICS and TCS for various Debye lengths. The top left panel presents the integrated CS for the $1^1S \to 2^3S$ transition and the top right panel presents the $1^1S \to 2^1S$ transition. We find that generally the integrated CS decreases as screening increases. The sharp rise at threshold is present for all Debye lengths, however, with the decrease of Debye length the CS maximum becomes smaller and broadens. In the resonance region, resonances can arise and so some variation in this region is likely. A smoothing routine has been applied to all integrated CS results near the $n = 2$ and $n = 3$ threshold region, where resonances are observed. To map out the resonance regions, a high-resolution energy grid would be required. Calculations with such a dense energy grid would require a large amount of computer time and is not in the scope of this study and

TABLE IV. 153-state CCC calculations static dipole polarizability (units of a_0^3) of the helium atom ground state, for various Debye lengths D (units of a_0). The polarizability is compared with the accurate calculations of Kar and Ho [18].

D	Polarizability	% Continuum contribution	[18]
∞	1.375	53	1.383
100	1.375	56	1.383
20	1.381	61	1.389
15	1.386	65	1.394
10	1.399	70	1.407
7.5	1.417	76	
5	1.466	87	1.474
2.5	1.731	100	1.74

will be performed elsewhere. Here the results for $D \geqslant 10a_0$ show little variation; however, results are significantly different for the $D = 5a_0$ case. At higher energies ($E \geqslant 100$ eV) we see that the results are indistinguishable for the $1^1S \to 2^3S$ transition. The $1^1S \to 2^1S$ transition show some variation at high energies.

The middle left panel of Fig. 8 presents the $1^1S \to 2^3P$ transition. Again, the results for $D \geqslant 10a_0$ show little variation; however, for the $D = 5a_0$ case results are significantly

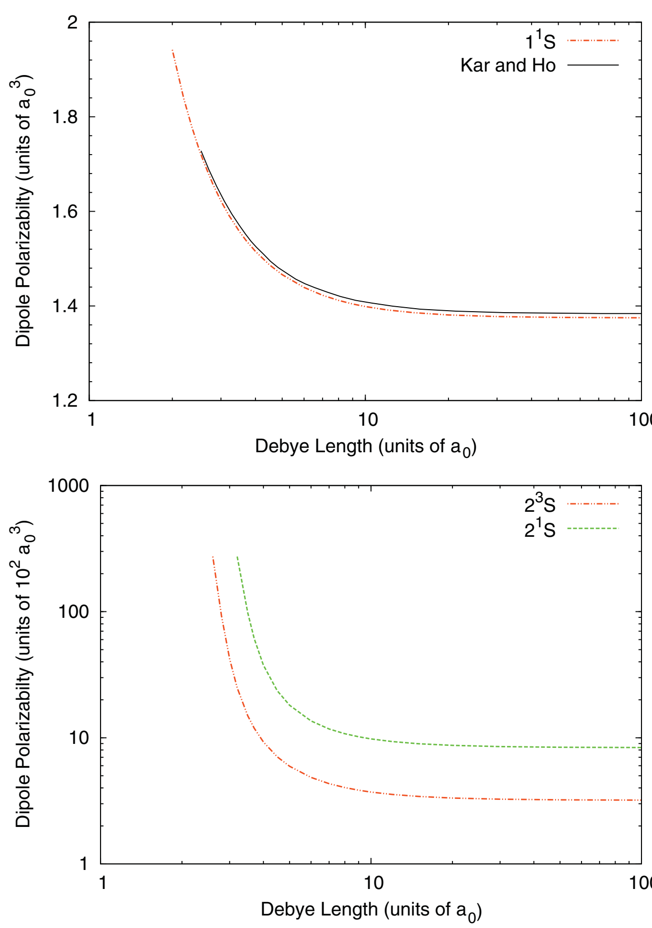

FIG. 5. (Color online) 153-state CCC calculations dipole polarizability for the helium atom ground, 2^3S and 2^1S states over a broad range of Debye lengths. CCC calculations compared with the accurate results of Kar and Ho [18].

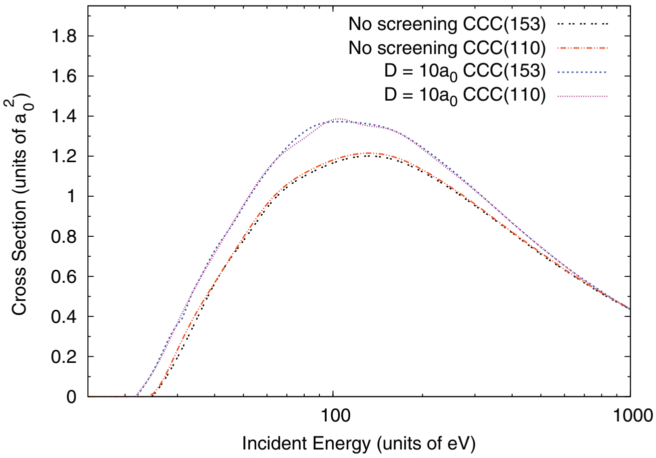

FIG. 6. (Color online) Electron-helium scattering from the ground-state state using 153-state CCC and 110-state CCC calculations. Total ionization cross sections presented for scattering off the ground state.

different, up to high energies. The next transition is $1^1S \to 2^1P$ transition, presented in the middle right panel. Here we see considerable changes across the entire energy range. As the Debye length decreases, the integrated CS peaks decrease, this is even observed for energies substantially away from the threshold region. Even at $E = 1000$ eV we see a significant variation in the integrated CS for all cases of $D < 100a_0$ presented. The transitions from the ground state to singlet states have integrated CS far broader than the transitions to triplet states. Similarities between the features of these results can be seen for other transitions presented; for example, $1^1S \to 2^1P$ and $1^1S \to 3^1P$, as seen in Fig. 9.

In Fig. 8, the D-dependence of excitation CS for dipole- and spin-allowed and dipole- or spin-forbidden transitions is considerably different. The strong D-dependence of the CS for $1^1S \to 2^1P$ transition in the entire energy region is a consequence of the changes of the electron wavefunctions when D varies. With decreasing D, the electron-density distribution of an s state significantly decreases and its maximum shifts toward larger radial distances, as seen in hydrogen (see Refs. [10,20]). Similar changes are exerted by wavefunctions of the states with higher l. For decreasing D the reduction of the magnitude of the $1^1S \to 2^1P$ integrated CS is a direct consequence of the reduction of wavefunction amplitudes for decreasing D. The observed shift of the maximum of the CS toward lower energies for decreasing D is a consequence of the shift of the maximum of the radial electron distribution of the initial state to larger radial distances, which are accessible for smaller energies. Finally, the lower threshold of the process for lower values of D is related to the decrease of energy difference between the 1^1S and 2^1P states when D decreases. The absence of a long-range part in the interaction for the dipole- and spin-forbidden transitions makes the sensitivity of the CS on screening much weaker, especially for the spin-forbidden transitions at high energies.

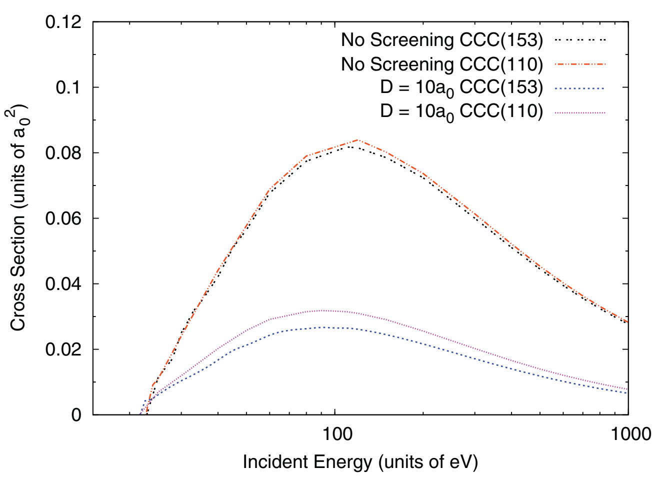

FIG. 7. (Color online) Electron-helium scattering from the ground-state state using 153-state CCC and 110-state CCC calculations. Integrated cross sections presented for the $1^1S \to 3^1P$ transition.

The bottom left panel of Fig. 8 presents the TICS of the helium atom ground state. We see agreement between both experiments [38,39] and the no screening calculations for all projectile energies considered. To date there is no other *ab initio* theory that is able to achieve such agreement over the entire energy range. The TICS peaks increase and shift to lower energies as the screening increases. At low collision energies such an increase is also enhanced by the increase of the amplitude of bound-state wavefunction at large (asymptotic) distances from the nucleus when D decreases [10,20]. At large collision energies, however, for which the CS is determined by the amplitude of bound-state wavefunction in the region close to the nucleus, the D dependence of the CS is determined by both the increase of number of pseudostates originating from the discrete spectrum and by the decrease of wavefunction amplitude with decreasing D in this region. This later effect should prevail for small values of D when the majority of pseudostates emerging from the discrete spectrum is close to exhaustion, as observed in Fig. 8 for the TICS of $D = 5a_0$. In the CCC method, the TICS is calculated as a sum of excitation-integrated CS to all open positive-energy pseudostates. This means that with decrease of Debye length D the TICS is constructed from increasing number of positive-energy-state-integrated CS, which individually decrease in value. The results presented for $D \leqslant 20a_0$ are visibly different at the lower energies but still converge to the other two calculations at the higher energies. Looking at the TICS peak maximum, we have concluded that the TICS are relatively insensitive compared to hydrogen [28] for realistic values of D that arise in Debye plasmas. For the TCS presented in the bottom right panel of Fig. 8 we see little variation of the results. The no-screening TCS are in agreement with the measurements of Kauppila *et al.* [40]. Generally, as the Debye length decreases the TCS decrease. It is not until we look at very low energies of the TCS that a significant change is seen, as discussed in Sec. III B 4.

The ground-state-excitation-integrated CS up to the $n = 3$ states are presented in Fig. 9 for various Debye lengths. All integrated CS in this figure are relatively small; hence, it is difficult to obtain convergence for these transitions. Results for these transitions are sensitive to the basis description,

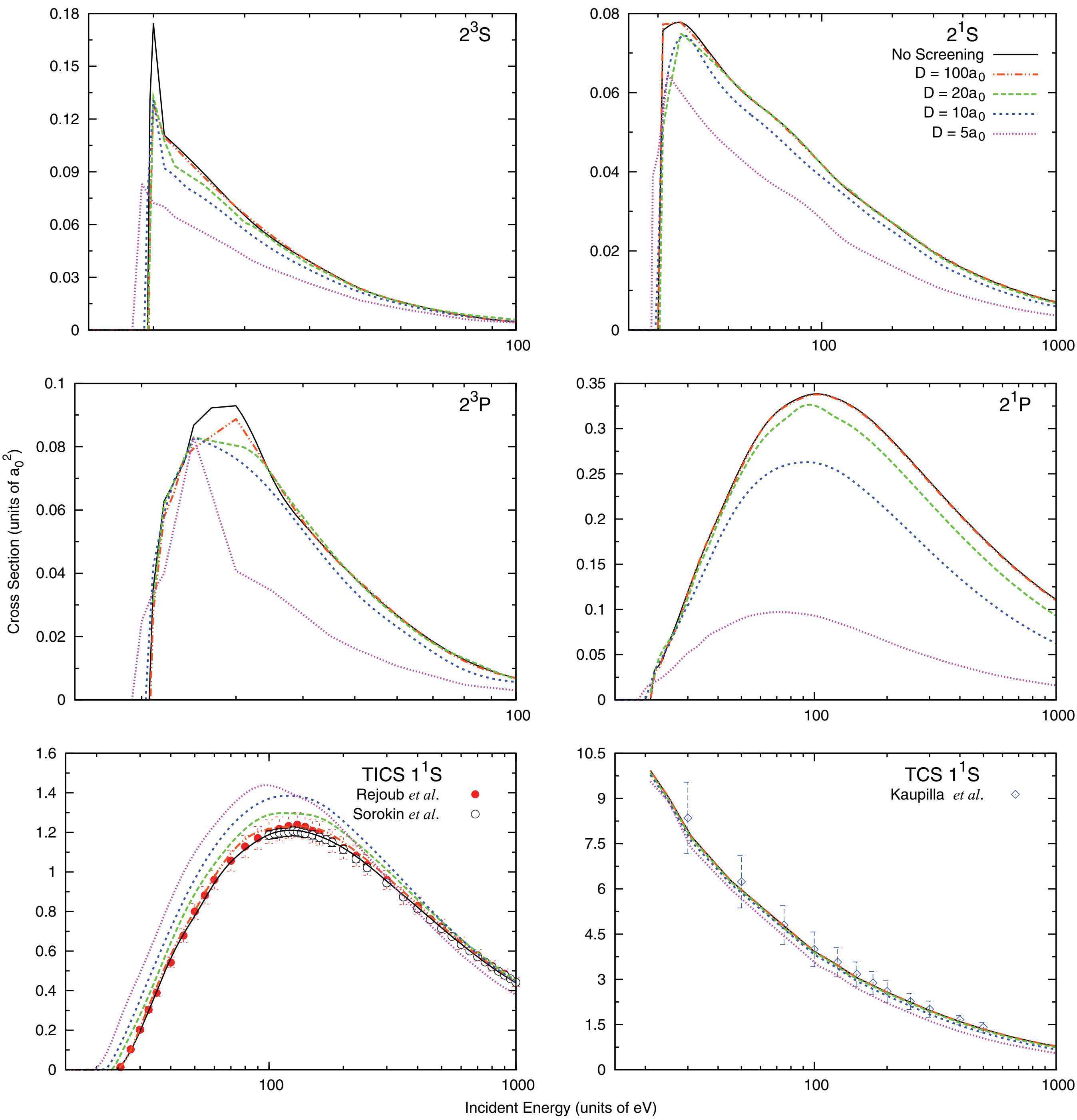

FIG. 8. (Color online) Electron-helium scattering from the ground-state state. Integrated cross sections presented for transitions up to the $n = 2$ states. Total ionization and total cross sections presented for scattering off the ground state. Experimental ionization measurements are due to Rejoub *et al.* [38] and Sorokin *et al.* [39]. Total cross-section measurements are due to Kauppila *et al.* [40].

number of partial waves, and choice of k grid. It is noted that the $n = 3$ states for $D = 5a_0$ are no longer bound and have merged into the continuum. The top left panel presents the integrated CS for the $1^1S \rightarrow 3^3S$ transition and the top right panel presents the $1^1S \rightarrow 3^1S$ transition. We find that generally the integrated CS decreases as screening increases. For the $1^1S \rightarrow 3^3S$ and $1^1S \rightarrow 3^1S$ transitions, the $D = 10a_0$ results has a maximum integrated CS of approximately half the no-screening results. The $1^1S \rightarrow 3^3S$ results are relatively insensitive to screening for $D \geqslant 15a_0$. The $1^1S \rightarrow 3^1S$ results have significant variation with respect to Debye length at energies far away from the threshold region.

The middle left panel of Fig. 9 is the plot of the $1^1S \rightarrow 3^3P$ transition integrated CS. As screening increases, the integrated

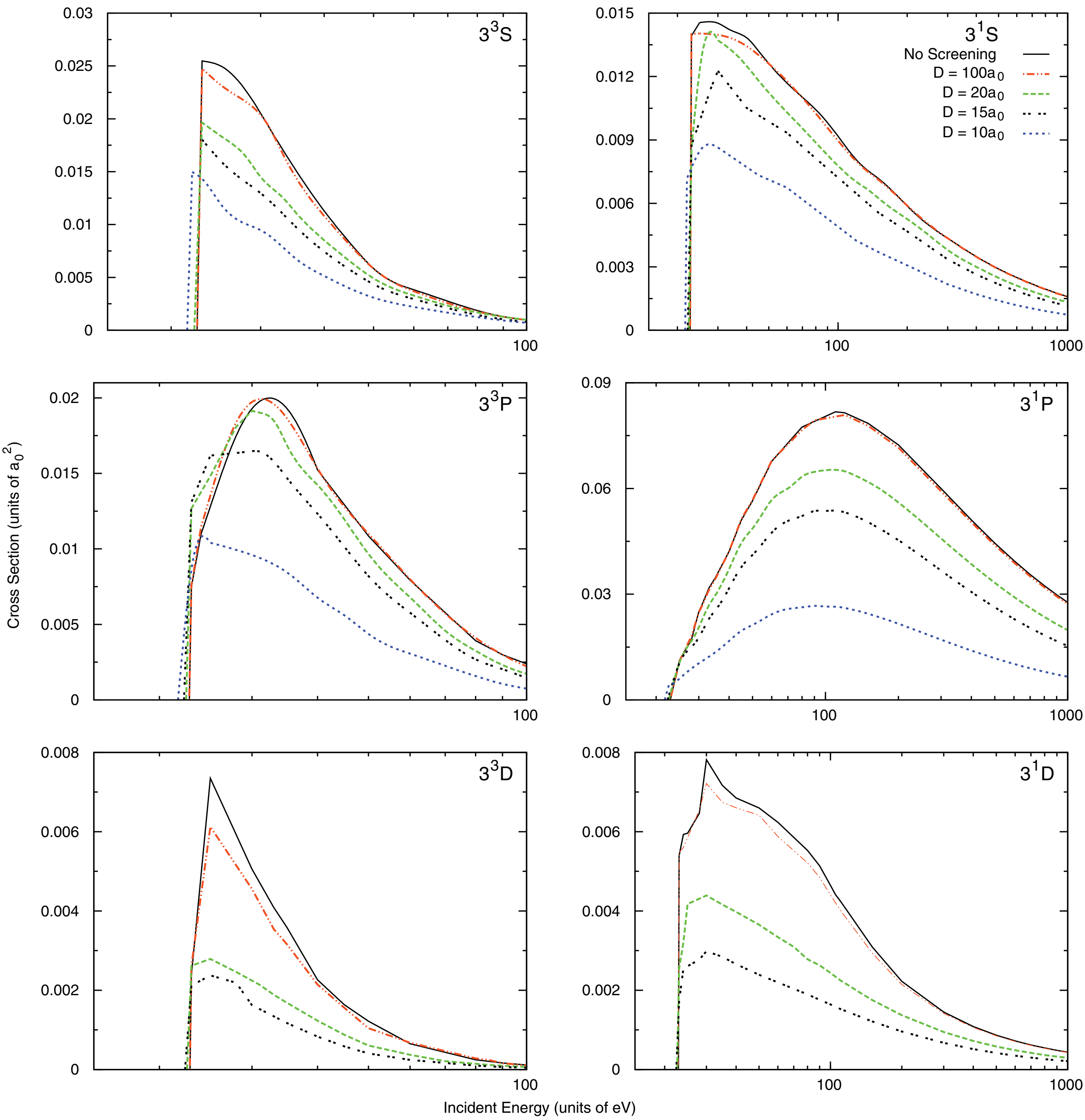

FIG. 9. (Color online) Electron-helium scattering from the ground state. Integrated cross sections presented for transitions up to the $n = 3$ states.

CS generally decrease. Results are relatively insensitive to screening for $D \geqslant 15a_0$. The middle right panel of Fig. 9 presents results for the $1^1S \to 3^1P$ transition. Here results are much more sensitive to the screening parameter D; even at $E = 1000$ eV integrated CS results still have a large variation.

The bottom left and right panels of Fig. 9 present the integrated CS for the transitions $1^1S \to 3^3D$ and $1^1S \to 3^1D$, respectively. Here we are dealing with very low integrated CS, which is reflected by the results sensitivity to the parameter D. For $D \leqslant 10a_0$ the $n = 3$, $l = 2$ states have moved into the continuum. As the screening increases the integrated CS decrease.

2. Excitation and ionization cross sections of the 2^3S state

In Fig. 10 we present integrated CS for scattering off the 2^3S state to the $n = 2$ shell and TCS of the 2^3S state. In the top

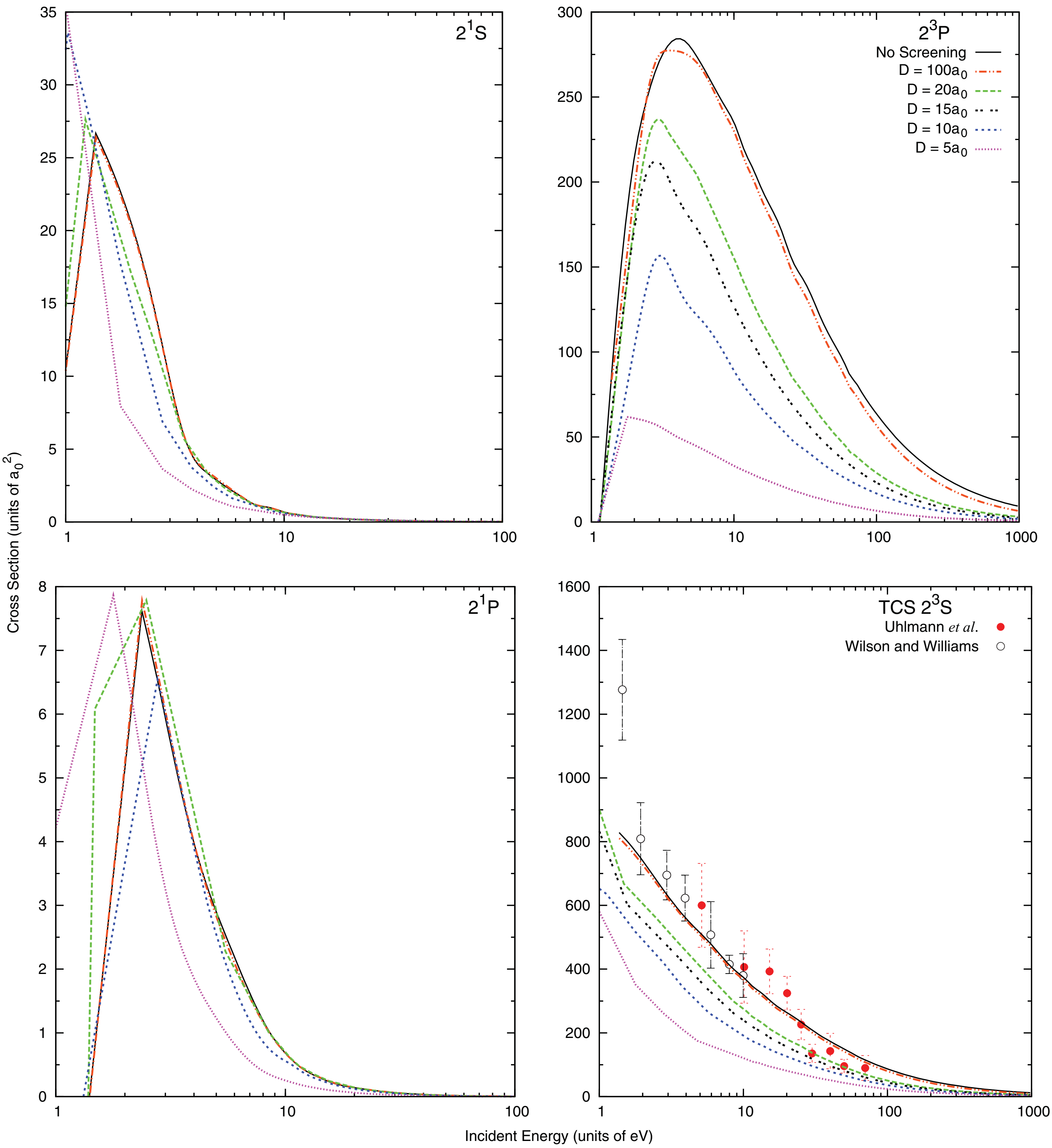

FIG. 10. (Color online) Electron-helium scattering from the 2^3S state. Integrated cross sections presented for transitions up to the $n = 2$ states and total cross sections of the 2^3S state. The experimental data is due to Uhlmann *et al.* [41] and Wilson and Williams [42].

and bottom left panels of Fig. 10, the integrated CS are shown for the excitation of $2^3S \rightarrow 2^1S$ and $2^3S \rightarrow 2^1P$, respectively. It is seen that the screening parameter D has a large influence over the shape and maximum of the CS at low energies. The top right panel presents the integrated CS for the $2^3S \rightarrow 2^3P$ transition. Here we see a significant change in results with respect to the Debye length. TCS of the 2^3S state are shown in the bottom right panel of Fig. 10. The no screening TCS are in agreement with data of Uhlmann *et al.* [41] and Wilson and Williams [42], within the uncertainties of the experiment.

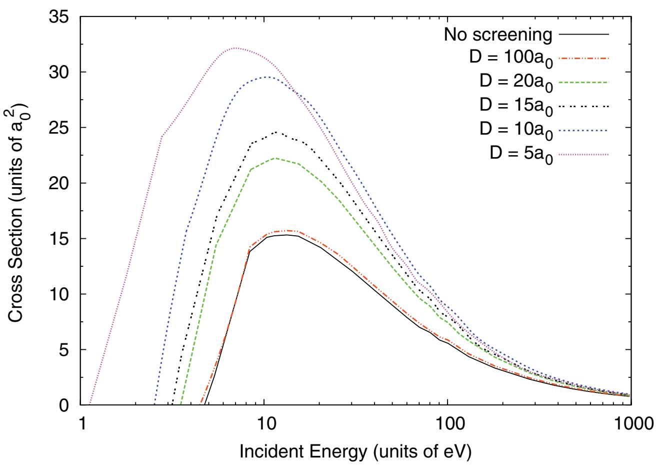

FIG. 11. (Color online) Electron-helium scattering from the 2^3S state total ionization cross sections.

We notice a significant variation of the TCS as the Debye length decreases, contrary to the TCS of the helium ground state; refer to Fig. 8. This is because the target wavefunctions decrease in amplitude, broaden, and become more diffuse as D decreases. The D-dependence of the target wavefunctions increases for electrons in higher n,l states. For all the processes presented in Fig. 10, the CS generally decreases as the D decreases.

In Fig. 11, we present the TICS of the 2^3S state. We first note that the threshold for ionization is relatively low (to the ground state) for all D. We see a wide variation of the TICS peak maximum and position with respect to Debye length. Again the TICS peaks shift toward lower energies and the TICS increase as the screening is increased. For a full discussion on the no-screening results see Ref. [32].

In Fig. 12 we present the integrated CS for scattering off the helium 2^3S state to the $n = 3$ shell. The top left and right panels show the integrated CS for the transitions $2^3S \to 3^3S$ and $2^3S \to 3^1S$, respectively. In both transitions we see that there is little difference in the integrated CS for energies above the threshold region. As the screening increases, the integrated CS decrease.

The middle left panel of Fig. 12 presents the integrated CS for the $2^3S \to 3^3P$ transition. Here we see a considerable difference in results across all energies, with respect to Debye length. The integrated CS for the $2^3S \to 3^1P$ transition is shown in the middle right panel. We see that the integrated CS above the threshold region is relatively insensitive to D. These transitions both show that as the Debye length decreases the integrated CS decreases.

In the bottom left and right panels of Fig. 12, we show the integrated CS for the transitions $2^3S \to 3^3D$ and $2^3S \to 3^1D$, respectively. Both these transitions show that as the Debye length decreases the integrated CS decreases. The integrated CS for the $2^3S \to 3^3D$ transition has a large variation in the low and intermediate energy range with respect to D. For the $2^3S \to 3^1D$ transition, the results are rather insensitive for all D above the threshold region.

3. Excitation and ionization cross sections of the 2^1S *state*

In Fig. 13 we present integrated CS for electron scattering off the 2^1S state to the 2^3P and 2^1P states, as well as TICS and TCS of the 2^1S state. In the top left panel, the integrated CS for $2^1S \to 2^3P$ transition is presented. There is little variation in results for all Debye lengths presented, except for the $D = 5a_0$ case. The $2^1S \to 2^1P$ transition is shown in the top right panel of Fig. 13. Here we see that the results have a large dependence on the Debye length. For both transitions we see a decrease of ICS as the screening is increased.

In the bottom left panel of Fig. 13, the TICS for the 2^1S state are presented. Just like for hydrogen [28], the TICS increase and the peak shifts toward lower energies as the Debye length decreases. A large variation is seen in the TICS, with the $D = 10a_0$ and $D = 5a_0$ cases having a maximum of approximately 2.5 times the maximum of the no-screening case. For higher energies at around $E \geqslant 300$ eV, the TICS start to become indistinguishable. TCS of the 2^1S state are shown in the bottom right panel of Fig. 13. Here we see a large variation of the TCS with respect to Debye length, contrary to the TCS of the ground state presented in Fig. 8. The no-screening results are in agreement with the experimental measurements due to Wilson and Williams [42]. The TCS decrease as the screening is increased for energies $E \geqslant 1$ eV.

Integrated CS are presented in Fig. 14 for transitions from the 2^1S state to the $n = 3$ states. The three left-hand-side panels correspond to the transitions $2^1S \to 3^3S$, $2^1S \to 3^3P$, and $2^1S \to 3^3D$, from top to bottom. All three of these cases show little difference in the integrated CS away from the threshold region, with respect to D. In the resonance region we see some variation in the results as expected. Generally the integrated CS decreases as the Debye length decreases.

From the right side panels of Fig. 14, we show the integrated CS of the transitions $2^1S \to 3^1S$, $2^1S \to 3^1P$, and $2^1S \to 3^1D$, from top to bottom. For the $2^1S \to 3^1S$ transition we see the CS peaks of the Debye cases $D = 20a_0$ and $D = 15a_0$ overlap with the no-screening and $D = 100a_0$ results. We notice that once that projectile has sufficient energy to ionize the target, the integrated CS then increases to a maximum (not including the resonance region), for all cases of D. The $2^1S \to 3^1P$ transition has a maximum CS in the intermediate energy range for the cases $D \geqslant 15a_0$, while for $D = 10a_0$ the integrated CS steadily decays for energies above the resonance region. For the $2^1S \to 3^1D$ transition we can see the nonmonotonic behavior of the integrated CS over the entire energy range, as Debye length decreases. Generally, the integrated CS decreases as the screening increases.

4. Elastic cross sections

Ghoshal and Ho [26] investigated low-energy electron scattering of the hydrogen atom. They found that at very low energies, below the $n = 2$ excitation threshold region, the elastic CS increases as the screening increases. We performed electron-helium CCC calculations in the very low energy region to see if we obtain the same behavior as seen in hydrogen [26].

In Fig. 15 we present the helium ground-state elastic-integrated CS. The CCC results for the no-screening case agree with the accurate calculations of Ref. [43]. It is seen

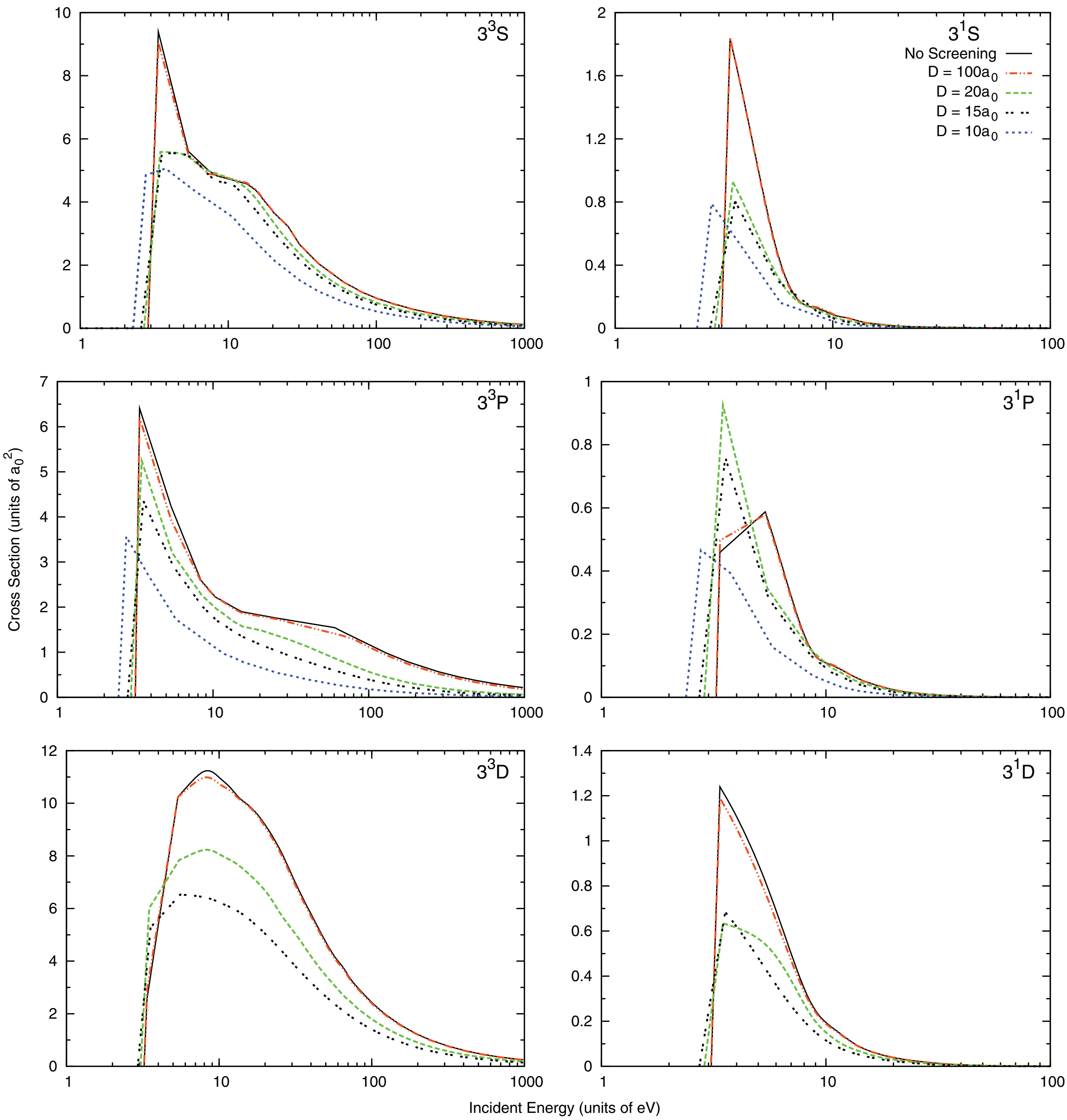

FIG. 12. (Color online) Electron-helium scattering from the 2^3S state. Integrated cross sections presented for transitions up to the $n = 3$ states.

that as we move to lower energies, the elastic CS increases as the Debye length decreases. For energies $E \leqslant 6$ eV we see that the integrated CS have some variation between the higher Debye length cases $D \geqslant 20a_0$ and the lower Debye length cases $D \leqslant 10a_0$. The nonmonotonic behavior seen in this energy region for elastic scattering was also obtained by Ghoshal and Ho [26]. This result is contradictory to the trend seen for other calculated integrated CS (as the screening increases the integrated CS generally decrease). This increase in the CS can be explained in two parts: as the screening increases the bound state wavefunction peak becomes smaller in amplitude, broadens, and becomes more diffuse. The second part of the explanation is considering the penetration of the projectile wavefunction with respect to its energy. At high

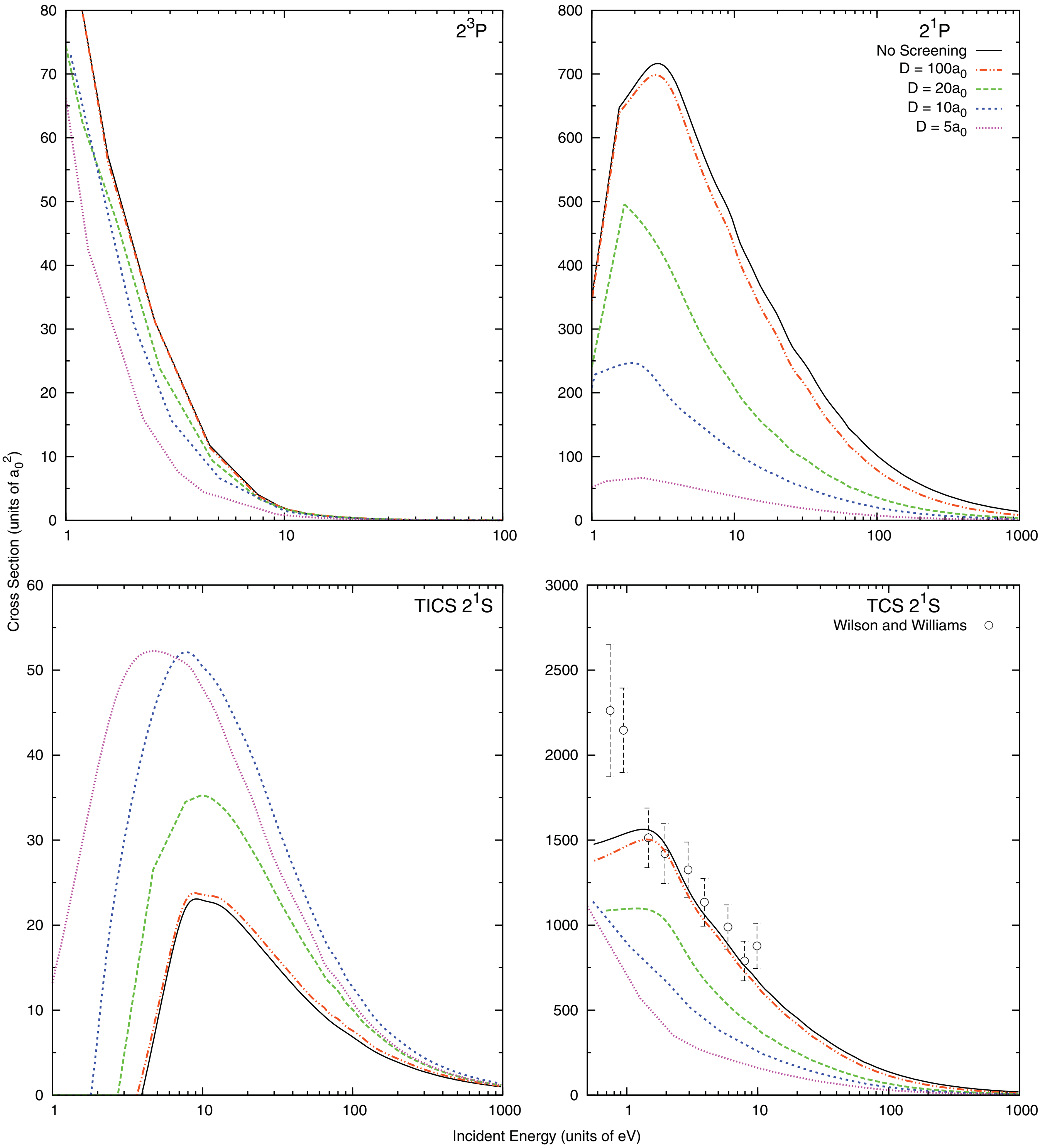

FIG. 13. (Color online) Electron-helium scattering from the 2^1S state. Integrated cross sections presented for transitions up to the $n = 2$ states. Total ionization and total cross sections presented for scattering off the 2^1S state. Experimental measurements are due to Wilson and Williams [42].

energies the projectile electron wavefunction penetrates deeply into the small radial range and is affected by the potential of the target defined by the bound-state wavefunction. Hence, at high energies the integrated CS decreases due to the amplitude of bound-state wavefunction decreasing as the Debye length decreases. At low energies the projectile wavefunction is distributed far from the origin and feels the potential of the target at large distances, which is described by the asymptotic

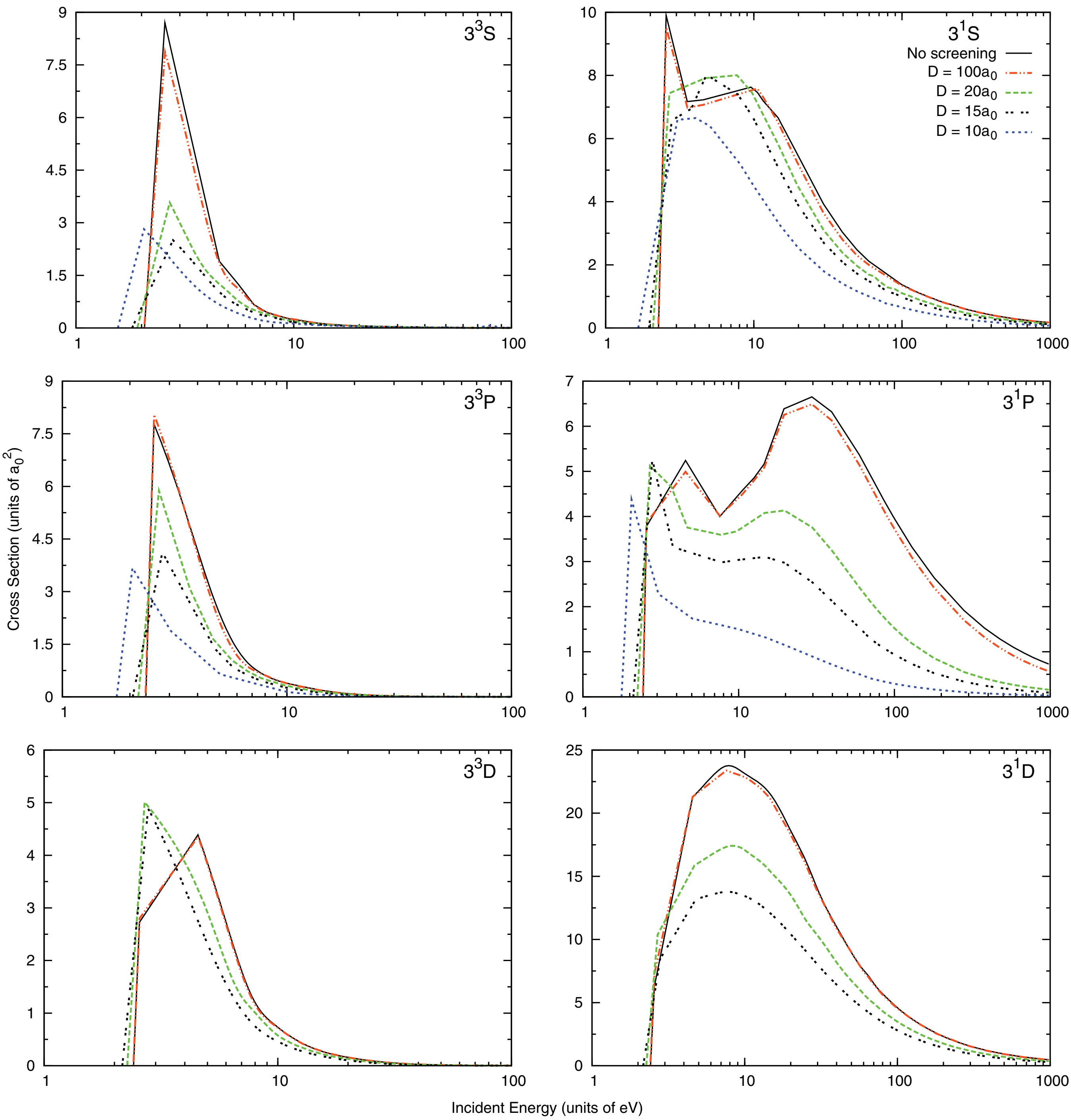

FIG. 14. (Color online) Electron-helium scattering from the 2^1S state. Integrated cross sections presented for transitions up to the $n = 3$ states.

part of the target wavefunction. This can be seen in Fig. 2 of Ref. [44]. Hence, at such low energies the CS is very sensitive to the tail of the ground-state wavefunction. Therefore, at low energies the CS increase is due to the diffusion of bound-state wavefunction, as D decreases.

MTCS of the ground state play an important role in the calculation of plasma transport properties. MTCS are defined by

$$\int_0^{\pi} d\Omega[1 - \cos(\theta)]\frac{d\sigma(\theta)}{d\Omega}, \tag{9}$$

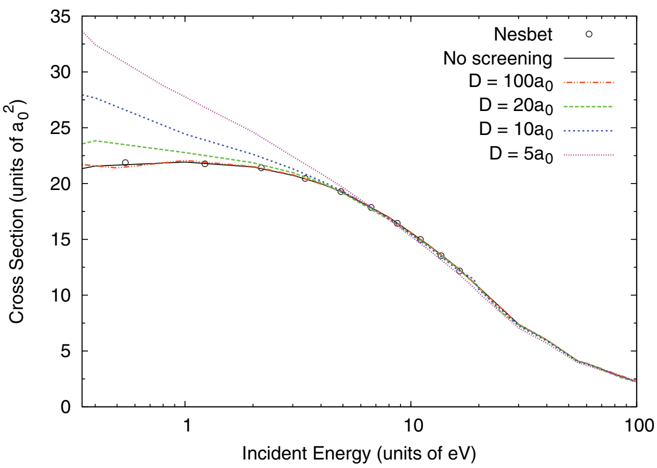

FIG. 15. (Color online) Electron-helium ground-state scattering elastic-integrated cross sections. Results compared with the calculations of Nesbet [43].

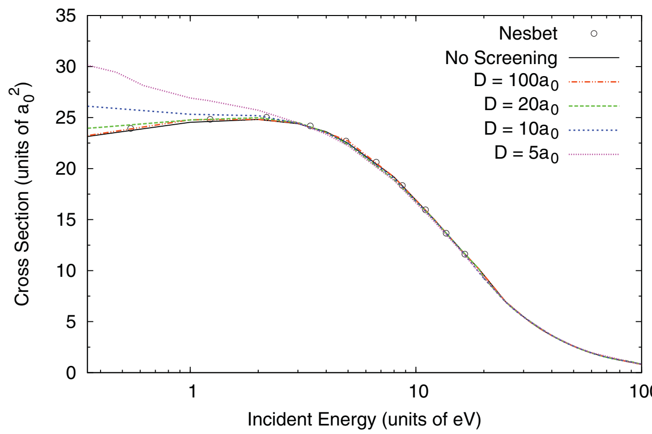

FIG. 16. (Color online) Electron-helium ground-state scattering for momentum transfer cross sections. Results compared with the calculations of Nesbet [43].

where $d\sigma(\theta)/d\Omega$ is the elastic differential CS and $d\Omega = 2\pi \sin(\theta)d\theta$ is the center-of-mass solid angle. In Fig. 16 we present the e$^-$-He ground-state scattering MTCS. Here we see a significant variation between the $D \leqslant 10a_0$ cases and the larger-D results at energies $E \leqslant 3$ eV.

IV. CONCLUSION

In this study we investigated electron-helium scattering in Debye plasmas using the CCC method. The Debye-Hückel potential was found to significantly effect the bound states and scattering processes of the metastable states. Generally, for scattering off the ground state a rather weak dependence of the presented CS was found for $D \geqslant 10a_0$. This can be explained by noting that helium is the most tightly bound atom (largest ionization potential) and consequently the least affected by the screening of the Coulomb interaction. In summary we found that as the screening increases, bound-state (ionic) energies increase, TICS increase, and excitation and TCS decrease. We also found that at low energies the elastic CS and MTCS increase as the Debye length decreases.

The calculated CS will be made available via the CCC database [45] and hopefully will be helpful for the modeling of Debye plasma transport and spectroscopic properties. Given the importance of resonance mapping near-threshold regions in plasma modeling, more calculations, with a higher energy resolution, are required. This will be the subject of our future research.

ACKNOWLEDGMENTS

This work was supported by the Australian Research Council and Curtin University. The in-kind contribution of the Resources of the Australian National Computational Infrastructure (NCI) Facility and the Western Australian node of iVEC are gratefully acknowledged.

[1] M. S. Pindzola, S. D. Loch, J. Colgan, and C. J. Fontes, Phys. Rev. A **77**, 062707 (2008).
[2] P. Beiersdorfer, Phys. Scr. T **134**, 014010 (2009).
[3] Y. Y. Qi, J. G. Wang, and R. K. Janev, Phys. Rev. A **78**, 062511 (2008).
[4] L. Zhang and P. Winkler, Int. J. Quantum Chem. **60**, 1643 (1996).
[5] S. Lorenzen, A. Wierling, H. Reinholz, and G. Ropke, Contrib. Plasma Phys. **48**, 657 (2008).
[6] S. Lorenzen, A. Wierling, H. Reinholz, and G. Ropke, Contrib. Plasma Phys. **51**, 349 (2011).
[7] A. Sil, S. Canuto, and P. Mukherjee, Adv. Quantum Chem. **58**, 115 (2009).
[8] D. Salzman, *Atomic Physics in Hot Plasmas* (Oxford University Press, Oxford, 1998), 1st ed.
[9] A. Sil, S. Bhattacharyya, and P. Mukherje, Int. J. Quantum Chem. **107**, 2708 (2007).
[10] F. J. Rogers, H. C. Graboske, and D. J. Harwood, Phys. Rev. A **1**, 1577 (1970).
[11] S. Kar and Y. K. Ho, Int. J. Quantum Chem. **106**, 814 (2006).
[12] S. Kar and Y. K. Ho, J. Quant. Spectrosc. Radiat. Transfer **109**, 445 (2008).
[13] S. Kar and Y. K. Ho, Phys. Rev. E **70**, 066411 (2004).
[14] S. Kar and Y. K. Ho, New J. Phys. **7**, 141 (2005).
[15] S. Kar and Y. K. Ho, Few-Body Syst. **40**, 13 (2006).
[16] J. K. Saha, S. Bhattacharyya, T. K. Mukherjee, and P. K. Mukherjee, J. Phys. B **42**, 245701 (2009).
[17] J. K. Saha, S. Bhattacharyya, T. Mukherjee, and P. Mukherjee, J. Quant. Spectrosc. Radiat. Transfer **111**, 675 (2010).
[18] S. Kar and Y. K. Ho, Int. J. Quantum Chem. **108**, 1491 (2008).
[19] J. M. Ugalde, C. Sarasola, and X. Lopez, Phys. Rev. A **56**, 1642 (1997).
[20] Y. Y. Qi, J. G. Wang, and R. K. Janev, Phys. Rev. A **80**, 032502 (2009).
[21] Y. Y. Qi, Y. Wu, J. G. Wang, and Y. Z. Qu, Phys. Plasmas **16**, 023502 (2009).

[22] S. B. Zhang, J. G. Wang, and R. K. Janev, Phys. Rev. Lett. **104**, 023203 (2010).
[23] S. B. Zhang, J. G. Wang, and R. K. Janev, Phys. Rev. A **81**, 032707 (2010).
[24] S. B. Zhang, J. G. Wang, R. K. Janev, and X. J. Chen, Phys. Rev. A **83**, 032724 (2011).
[25] B. Saha, P. K. Mukherjee, and G. H. F. Diercksen, Astron. Astrophys. **396**, 337 (2002).
[26] A. Ghoshal and Y. K. Ho, J. Phys. B **43**, 045203 (2010).
[27] G. J. Hatton, N. F. Lane, and J. C. Weisheit, J. Phys. B **14**, 4879 (1981).
[28] M. C. Zammit, D. V. Fursa, and I. Bray, Phys. Rev. A **82**, 052705 (2010).
[29] M. Zammit, D. Fursa, and I. Bray (in press), doi: 10.1016/j.chemphys.2011.04.034.
[30] D. V. Fursa and I. Bray, Phys. Rev. A **52**, 1279 (1995).
[31] I. Bray and D. V. Fursa, Phys. Rev. A **54**, 2991 (1996).
[32] D. V. Fursa and I. Bray, J. Phys. B **30**, 757 (1997).
[33] I. Bray and A. T. Stelbovics, Phys. Rev. Lett. **69**, 53 (1992).
[34] I. Bray and A. T. Stelbovics, Phys. Rev. A **46**, 6995 (1992).
[35] I. Bray and A. T. Stelbovics, Phys. Rev. Lett. **70**, 746 (1993).
[36] I. J. Thompson and A. R. Barnett, Comp. Phys. Commun. **36**, 363 (1985).
[37] C. E. Moore, *Atomic Energy Levels as Derived from Analyses of Optical Spectra*, Circ. No. 467, Vol. 1 (Natl. Bur. Stand., US GPO, Washington, DC, 1949).
[38] R. Rejoub, B. G. Lindsay, and R. F. Stebbings, Phys. Rev. A **65**, 042713 (2002).
[39] A. A. Sorokin, I. L. Beigman, S. V. Bobashev, M. Richter, and L. A. Vainshtein, J. Phys. B **37**, 3215 (2004).
[40] W. E. Kauppila, T. S. Stein, J. H. Smart, M. S. Dababneh, Y. K. Ho, J. P. Downing, and V. Pol, Phys. Rev. A **24**, 725 (1981).
[41] L. J. Uhlmann, R. G. Dall, A. G. Truscott, M. D. Hoogerland, K. G. H. Baldwin, and S. J. Buckman, Phys. Rev. Lett. **94**, 173201 (2005).
[42] W. G. Wilson and W. L. Williams, J. Phys. B **9**, 423 (1976).
[43] R. K. Nesbet, Phys. Rev. A **20**, 58 (1979).
[44] Y. Y. Qi, J. G. Wang, and R. K. Janev, Phys. Rev. A **80**, 063404 (2009).
[45] I. Bray, Y. Ralchenko, K. Lewis, and ITP Group Curtin University, *CCC database* (2009).